ADVANCED FUNCTIONAL MATERIALS
www.afm-journal.de

$Nd_2(S, Se, Te)_3$ Colloidal Quantum Dots: Synthesis, Energy Level Alignment, Charge Transfer Dynamics, and Their Applications to Solar Cells

Qinghua Li, Xiao Jin, Ying Yang, Haonan Wang, Haijiao Xu, Yuanyuan Cheng, Taihuei Wei, Yuancheng Qin, Xubiao Luo, Weifu Sun,* and Shenglian Luo**

Novel and less toxic quantum dot (QD) semiconductors are desired for developing environmentally benign colloidal quantum dot solar cells. Here, the synthesis of novel lead/cadmium-free neodymium chalcogenide $Nd_2(S, Se, Te)_3$ QDs via solution-processed method is reported for the first time. The results show that small-bandgap semiconductor QDs with a narrow size distribution ranging from 2 to 8 nm can be produced, and the wide absorption band can be achieved by the redshift owing to the size quantization effect by controlling the initial loading of chalcogenide precursors. By analyzing the band structure of QDs and the energy level alignment between QDs and TiO_2, the influence of energy offset between the conduction band edges of QDs and TiO_2 on the charge transfer dynamics and photovoltaic performance of QD solar cells (QDSCs) is investigated. It is revealed that among the three types of QDs studied, Nd_2Se_3 QDSCs with the smallest energy offset exhibit the best performances and a decent power conversion efficiency of 3.19% is achieved. This work clearly demonstrates the promising potentials of novel rare earth chalcogenide quantum dots in photovoltaic applications.

1. Introduction

Colloidal quantum dots (QDs) have received considerable attention owing to their size-tunable bandgap over a wide range of energies, high photoluminescence quantum yield, low-cost solution processability, and their widely tunable absorption and emission.[1] Because of these features, QDs have been actively investigated for use in optoelectronic devices ranging from solar cells, light emitting devices,[2] chemical sensing,[3] and biomedical fluorescence labels.[4] Among these potential applications, the realization of low-cost and high efficiency solar cells has been of particular interest due to their potential in meeting increasing social demands for clean and sustainable energy resources. Although much progress over the past few years has been made in the QD-based solar cells (QDSC),[5] nonetheless the power conversion efficiency (PCE) typically lags behind dye-sensitized solar cells[6] and perovskite solar cells.[7] One of the main reasons responsible for the low PCE of solid-state QDSCs[8] is because the significant fraction of the photon energy is lost during the charge transfer process, at least partly due to the mismatched energy offset between the lowest unoccupied molecular orbital (LUMO) of the low-bandgap semiconductor QD donor and the wide-bandgap semiconductor acceptor (e.g., TiO_2). Thus, it is necessary to form appropriate energy level diagram between electron donor and acceptor in virtue of adjusting either particle size or compositions.[8b,9] So far, the understanding of the factors such as the efficient charge generation, separation, transfer, and electron–hole recombination[10] that limit their performances has greatly improved.[11] For example, advanced time-resolved spectroscopies[12] have been adopted to explore the photophysical mechanisms. However, to the best of our knowledge, the type of QD semiconductors that have been exploited for the third-generation thin-film solar cells is limited so far and more endeavors are still needed to understand the in-depth underlying physics within or at the interface of QDs/TiO_2 bulk heterojunction (BHJ).

Since the first demonstration of QDSC,[13] in which quantum dot semiconductors harvest visible light energy and a wide-bandgap semiconductor (e.g., TiO_2) acts as electron extraction

Dr. Q. Li, Dr. X. Jin, Y. Yang, H. Wang, H. Xu
Jiangxi Engineering Laboratory
for Optoelectronics Testing Technology
Nanchang Hangkong University
Nanchang 330063, P. R. China
E-mail: qhli@hqu.edu.cn
Dr. Y. Cheng, Dr. Y. Qin,
Prof. X. Luo, Prof. S. Luo
Key Laboratory of Jiangxi Province
for Persistent Pollutants Control
and Resources Recycle
Nanchang Hangkong University
Nanchang 330063, P. R. China
E-mail: sllou@hnu.edu.cn
Prof. T. Wei
Department of Physics
National Chung-Cheng University
Chia-Yi 621, Taiwan, Republic of China
Dr. W. Sun
Centre for Advanced Materials Technology (CAMT)
School of Aerospace
Mechanical and Mechatronic Engineering J07
The University of Sydney
New South Wales 2006, Australia
E-mail: weifu.sun518@gmail.com

DOI: 10.1002/adfm.201503433

media in a photoactive layer,[5c] there have been numerous attempts to improve the device performance by either optimizing the device architecture or synthesizing new materials. Size quantization effect allows one to tune the visible response and vary the band energies to match the sun's wide spectrum, thus proving driving forces to initiate charge injection from excited QDs into electrode surfaces.[14] So far, emphasis has been placed on small bandgap semiconductor QDs such as CdS, PbS, CdSe, PbSe, etc, and exploiting their synthetic strategies and the photophysical properties.[10b,15] Since the very initial initiative for the development of solar cells is to explore environmentally clean alternate energy resources whereas currently QDSCs are mainly focused on highly toxic cadmium and lead chalcogenides, therefore, on one hand, it becomes necessary to synthesize new semiconductor quantum dot materials. To date, researchers have largely restricted their QDs within relative narrow limits, such as II–VI,[16] IV–VI,[10b,17] carbon[18] and silicon[19] semiconductors, the exploring of Pb and/or Cd-free and relatively green QDs (e.g., neodymium chalcogenide) have been rarely touched so far.

In order to explore and develop new QD materials and also better understand the underlying working principles of these photovoltaic devices, herein, we target at and report the first synthesis of the less toxic rare earth chalcogenides $Nd_2(S, Se, Te)_3$ QDs via a simple and low-cost hydrothermal method to expand the range of quantum dot semiconductors in the quest of acquiring better energy level matching and reducing energy offset in all-solid-state QDs BHJs. Then, the structure, morphology, and composition of the prepared QD materials are characterized using transmission electron microscopy (TEM), X-ray diffraction (XRD), inductively coupled plasma atomic emission spectroscopy (ICP-AES), energy dispersive X-ray spectroscopy (EDS), and X-ray photoelectron spectroscopy (XPS), etc. Finally, the applications to photovoltaic devices of these three different types of QDs are proposed and in order to expound these differences, the optical properties, energy level diagram, and charge transfer dynamics of the novel $Nd_2(S, Se, Te)_3$ QDs within the solid-state solar cells, etc., are separately studied.

2. Results and Discussion

The prepared colloidal $Nd_2(S, Se, Te)_3$ QDs are characterized by TEM and high-resolution TEM (HR-TEM). The morphologies of the prepared QDs are shown in **Figure 1**. An estimated distance spacing of 0.322, 0.290, and 0.313 nm was roughly evaluated from the lattice fringes for $Nd_2(S, Se, Te)_3$ QDs,

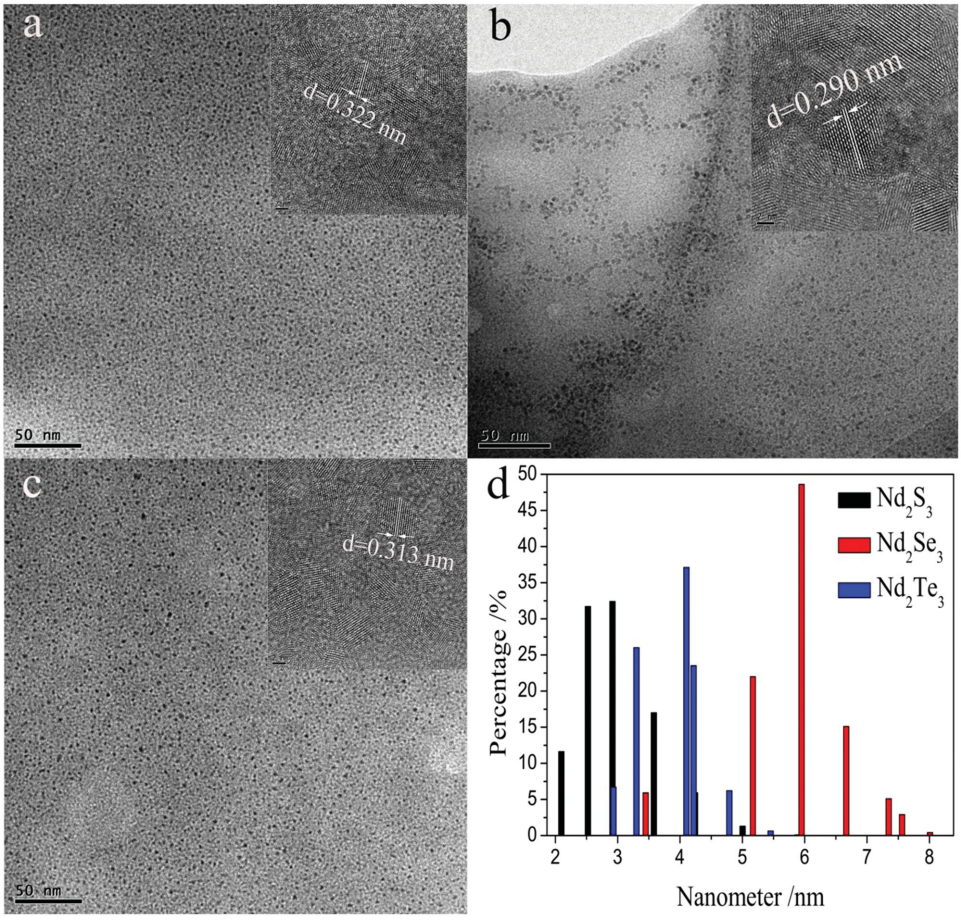

Figure 1. Structural characterizations of $Nd_2(S, Se, Te)_3$ QDs. a) The TEM images of Nd_2S_3, b) Nd_2Se_3 , c) Nd_2Te_3 QDs, and d) the histogram of the size distributions of the colloidal QDs. The insets highlight the HR-TEM images of $Nd_2(S, Se, Te)_3$ QDs, respectively.

respectively. These observed *d*-spacing values are consistent with cubic structure of $Nd_2(S, Se, Te)_3$ QDs.[20] The statistical size distributions of $Nd_2(S, Se, Te)_3$ QDs are roughly calculated by counting from at least 20 HR-TEM images and the results are displayed in Figure 1d. The diameter of $Nd_2(S, Se, Te)_3$ QDs falls within the narrow nanometer domain of about 2–3.5, 5–7, and 3–4.5 nm, respectively and the corresponding average diameters are 2.9 (33%), 5.9 (48%), and 4.2 (37%) nm for Nd_2S_3, Nd_2Se_3, and Nd_2Te_3 QDs, respectively.

In order to determine the final concentration of each element, we tested transparent solution of the QDs using ICP-AES. By linear fit of the ICP peak intensity of standard liquid, the relationship between the peak intensity and the concentration is revealed in **Figure 2**. The final residual concentrations of the elements are shown in Table S1 in the Supporting Information. After equivalent mathematical conversion, the final atomic ratios of Nd:S, Nd:Se, and Nd:Te for the three optimized QDs are determined to be 2:3.1, 2:3.2, and 2:2.9, respectively. This is in good agreement with those obtained from the EDS analysis (Figure S1, Supporting Information). That is, the atomic ratios of Nd:S, Nd:Se, and Nd:Te are calculated to be 2:3.13, 2:3.4, and 2:3.3, respectively.

To investigate the valence states of the composing elements and the final composition of QDs, XPS measurements were performed. As shown in **Figure 3**a, all of the QDs exhibit the 3d band of Nd clearly, which consists of the 3d5/2and 3d3/2 peaks and satellites. The asymmetric 3d5/2 and 3d3/2 profiles with shoulders are Gauss-fitted to locate the satellite peaks from the 3d main peaks. The observation of satellite peaks in Nd is attributed to predominant mixing of 4f levels.[21] Meanwhile, the main components, i.e., Nd 3d5/2 (983.2 eV) and Nd 3d3/2 (1005.6 eV) peaks with a spin-orbit coupling (Δ) of 23.4 eV, are comparable to those observed in the related systems.[22] Therefore, the Nd 3d peaks are unanimously assigned to the ground final state of Nd^{3+} ion, which remain well described with a relatively pure $4f^3$ valence configuration.[23] Besides, Figure 3b reveals that the 2p3/2 and 2p1/2 peaks lie in the range of 160–164 eV, suggesting its S^{2-} state.[24] The Se 3d5/2, Te 3d5/2, and Te 3d3/2 binding energies are observed at 54.4, 571.6, and 581.6 eV, respectively, which confirms the existence of Se^{2-} and Te^{2-} (Figure 3c,d).[5c,25] Finally, the composition of the QDs could be determined as $Nd_2(S, Se, Te)_3$. It is worth mentioning that the Se 3d spectrum should have two peaks for Se 3d3/2 and 3d5/2. However, because of the comparable intensity (4:6), the close peak positions (3d3/2 at 55.36 eV, 3d5/2 at 54.49 eV) are so close to each other,[26] that the two peaks are not easy to be distinguished from each other. In particular, the width of each peak is about 0.77 eV, which is close to the peak–peak difference. As a result, the Se 3d3/2 and 3d5/2 peaks are prone to combine to a single peak, thus leading to a broader width (≈2.0 eV) in the current Se 3d spectrum. Similar XPS Se 3d results are obtained in some related QDs.[9e,27]

As confirmed by XRD (**Figure 4**), the crystal structures of the Nd_2S_3, Nd_2Se_3, and Nd_2Te_3 QDs have been assigned as cubic, cubic, and orthorhombic structures, respectively. These are consistent with the standard patterns of JCD 00-026-1450, 00-019-0823, and 00-018-0866, respectively. Distance spacings obtained from XRD patterns, i.e., $d = 0.348$, 0.278, and 0.298 nm

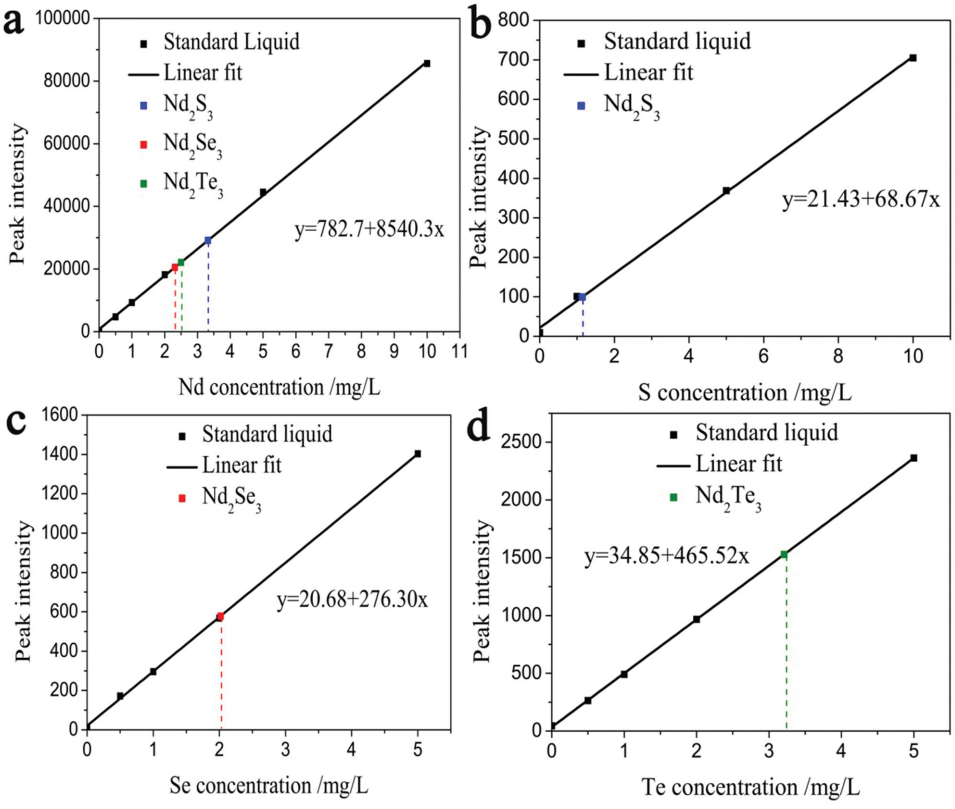

Figure 2. Linear fits of the ICP peak intensity for the standard liquid as a function of different concentrations of a) Nd, b) S , c) Se, and d) Te.

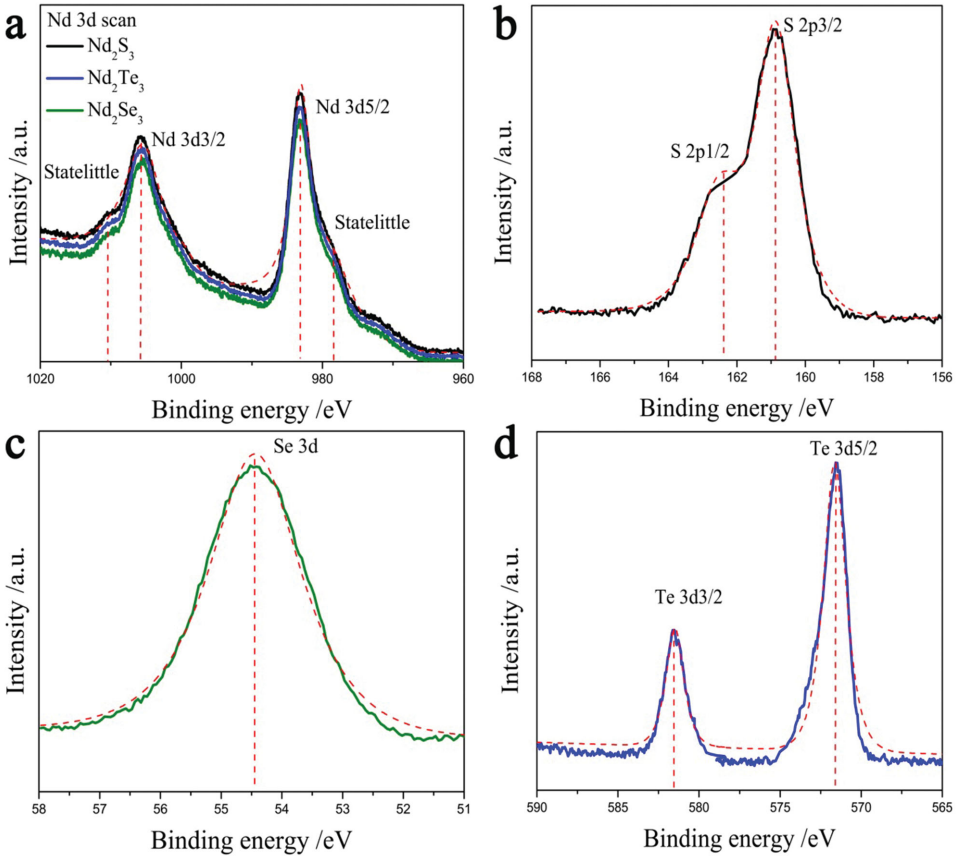

Figure 3. XPS spectra of the QDs. a) XPS spectra of Nd 3d for $Nd_2(S, Se, Te)_3$ QDs, b) XPS spectrum of S 3d for Nd_2S_3 QDs, c) XPS spectrum of Se 3d for Nd_2Se_3 QDs, and d) XPS spectrum of Te 3d for Nd_2Te_3 QDs.

corresponding to the characteristic (211), (310), and (400) peaks pattern, are in agreement with those from their individual standard cards, i.e., d = 0.322, 0.290, and 0.313 nm for $Nd_2(S, Se, Te)_3$, respectively.

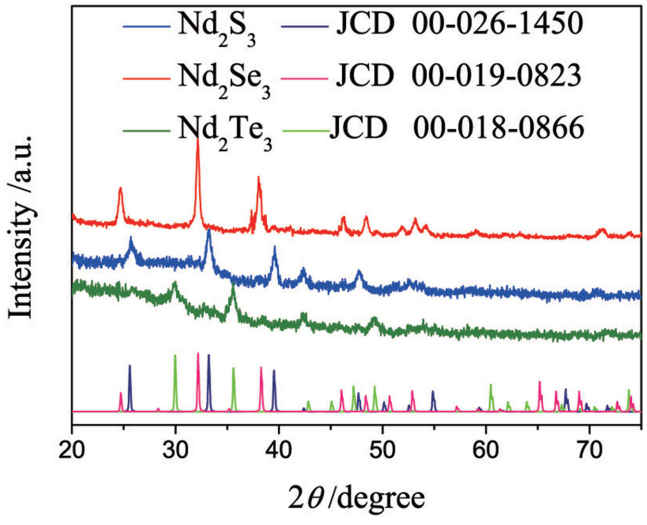

Figure 4. XRD patterns of the three optimized QDs and the corresponding standard patterns.

The effect of the different molar ratio of the Nd to S, Se, and Te precursors on the optical properties of colloidal QDs in water was studied and the results are shown in **Figure 5**. As displayed in Figure 5a, all QDs have exhibited a broad absorption band ranging from 300 to 600 nm and the band gaps of the QDs are dependent on the molar ratios. It is found that significant redshifts of the absorption band edge occur with increasing the loading amounts of S, Se, and Te precursors. Similar trends are also observed with photoluminescence (PL) spectra under light excited at 400 nm as demonstrated in Figure 5b. A significant redshift of the PL is clearly shown with increasing the initial loading, the PL peak gradually shifts to a longer wavelength and a wide emission spectrum is expanded to the visible range of 410–600 nm. Such shifts to longer wavelengths could be ascribed to the increase in size of QDs as observed and discussed elsewhere.[14a,28] But note that the surface structure such as surface defects or surface engineering by ligands could also take part in affecting PL characteristics, thus giving rise to similar phenomenon.[9e,29] However, it is hard to experimentally distinguish whether the emission originates from the intrinsic electronic states that are related to the QD sizes, or from the defect states depending on the QD surface structures and/or ligand agents. This area awaits systematic effort to be invested in future such as density functional theory calculations. Moreover, the intensity of the emission peaks gradually falls off and the broad emission spectra gradually disappear after further

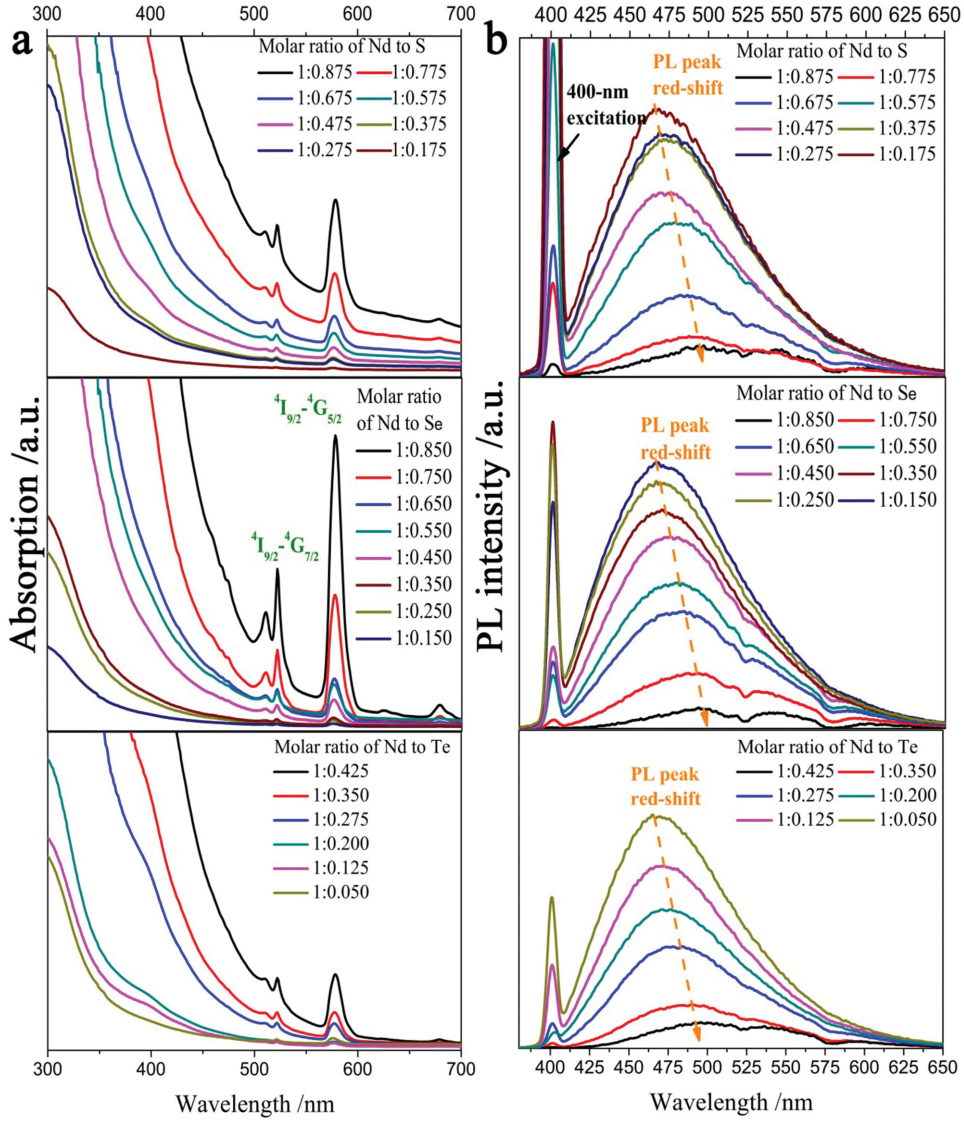

Figure 5. Optical properties of $Nd_2(S, Se, Te)_3$ colloidal QDs. a) The UV–vis absorption spectra and b) PL emission spectra of $Nd_2(S, Se, Te)_3$ QDs with different initial loadings of chalcogenide precursors.

increasing the loading amount of precursors, which is attributed to the expected Ostwald ripening accompanied by the introduction of unpredictable defect states during the growth of QDs, thus leading to the quenching of QD PL intensity.[30] Moreover, all of the UV–vis absorption spectra for colloidal $Nd_2(S, Se, Te)_3$ QDs show a strong absorption peak centered at 587 nm while two weak peaks are observed at 512 and 528 nm, which correspond to the direct excitation of the $^4I_{9/2}\rightarrow{}^4G_{5/2}$ (587 nm), $^4I_{9/2}\rightarrow{}^4G_{9/2}$ (512 nm), and $^4I_{9/2}\rightarrow{}^4G_{7/2}$ (528 nm) transitions of the Nd^{3+} ions, respectively.[31] However, no obvious excitonic absorption peaks have been observed, even in dilute solutions. This phenomenon may be ascribed to the high degree of QD–QD electronic coupling, and defect states that are generally associated with disorder or imperfect QD surfaces,[32] which can bind excitons to compete with excitonic absorption and weaken excitonic absorption peaks.[33] As newly developed QD materials, surface defect or disorder exists, a hint of which can be given from the XRD results and relatively still low quantum yield (Figure S3, Supporting Information). Similar phenomenon has been observed in QD systems reported elsewhere.[32a,34] Furthermore, Figure S2a in the Supporting Information shows the photograph of the QDs under natural light, exhibiting emission colors from opaque to dark brown, whereas Figure S2b in the Supporting Information displays the photograph of emission colors under 365 nm UV excitation from bright blue to deep green, indicating a significant bathochromic shift in the emission band that stems from the well-established size quantization effect by the dependence of the band gap on the particle size. Additionally, the influence of the precursor ratio in controlling the PL quantum yield (QY) of the three QDs is shown in Figure S3 in the Supporting Information. In all cases, the QY decreases with the ratio of neodymium to chalcogenide precursor (S, Se, or Te), indicating that the growth of all nanocrystals becomes a disadvantage

stage after forming the initial nucleation. Although the absorption band edges decrease with the molar ratio, which may lead to enhanced light absorption, however, their PL QYs become quite low and those absorbed photons tend to convert to heat without contributing to electric current. It is difficult to simultaneously achieve the maximum fluorescence quantum yield and the largest absorption at this stage of development. Our results demonstrate that neither the QDs with the maximum absorption band edge nor the QDs with maximum emission intensity deliver the best photovoltaic performances. Instead, the QDs with modest absorption band edge and balanced QY (19.3%, 24.2%, and 20.8% for Nd_2S_3, Nd_2Se_3, and Nd_2Te_3, respectively) deliver the best photovoltaic performances of the corresponding all-solid-state QDSCs. Finally, the external quantum efficiency (EQE) measurements for the three optimized QDSCs were performed (Figure S4, Supporting Information). The EQE spectra closely match the corresponding absorption spectra for each QD. A notable shoulder peak located at about 580 nm is observed in the EQE spectra, which is attributed to the strong characteristic absorption of Nd species. The Nd_2Se_3 QDSC displays wider EQE spectrum (up to 650 nm) and much higher EQE values than other QDs in the whole photoresponse range. This may be associated with its smaller bandgap and faster charge transfer rate as will be discussed below.

Next, the potential application of synthesized Nd_2(S, Se, Te)$_3$ QDs to solar cells was demonstrated by fabricating QDSCs, in which Nd_2(S, Se, Te)$_3$ QDs are used as electron donor and TiO_2 acts as electron acceptor, through a subsequent deposition or coating of QDs/TiO_2 BHJ, poly (3,4-ethylenedioxylenethiophene)-poly(4-stylene sulfonic acid) (PEDOT:PSS) and Pt electrode on fluorine-doped tin oxide (FTO) substrate as demonstrated in **Figure 6**c. The morphologies of pure TiO_2 and TiO_2/QDs BHJ films are shown in Figure 6a,b, respectively. It can be observed from Figure 6a that the surface of the TiO_2 acceptor (particle diameter of about ≈20–30 nm) clearly exhibits a loose and porous structure, which, on one hand, is prone to readily adsorb QDs in the porosity[35] in virtue of intermolecular attractive forces[36]; on the other hand, favors the p–n contact for BHJ and offers channels for Nd_2(S, Se, Te)$_3$ QDs across the acceptor layer. It is worth mentioning that the GSH-modified QDs can bring about –COOH functional groups, which favors the QDs to anchor onto the TiO_2 surface. In contrast, the morphology of TiO_2/QDs BHJ (Figure 6b) indicates that the QDs have been uniformly penetrated into or covered on the TiO_2 acceptor layer. To further characterize the structure of TiO_2/QDs BHJ, the cross-sectional scanning electron microscope (SEM) image of BHJ is shown in Figure 6e, in which different layers and their individual thickness of FTO, BHJ can be clearly distinguished, and the thickness of BHJ including n-TiO_2 and p-QDs is estimated to be about 250 nm. As highlighted in the insert of Figure 6e, the porous structure of bare TiO_2 layer is clearly displayed. Besides, cross-sectional X-ray elemental mapping further confirm that Nd_2Se_3 QDs permeate well into the TiO_2 as shown in Figure S5 in the Supporting Information. And it also reveals that the thickness of Nd_2Se_3 QDs is about 400 nm, which is slightly thicker than that of TiO_2 and further confirms that many QDs should have covered or deposited both on the TiO_2 surface and trapped into porous TiO_2 layer.

Initially, we chose the QDs with different fluorescence emission to fabricate solid-state QDSCs for photocurrent–voltage (J–V) characterization as shown in Figure S6 in the Supporting Information and the photovoltaic parameters of QDSCs are summarized in Table S2 in the Supporting Information. Unfortunately, neither the QDs with the maximum absorption band edge nor the QDs with maximum emission intensity deliver best photovoltaic performances. Instead, the QDs with modest absorption band edge and considerable emission intensity deliver the best photovoltaic performances. In detail, the optimized ratios of neodymium to chalcogenide precursors (S, Se, and Te) are found to be 1:0.675, 1:0.650, and 1:0.275, respectively. As mentioned above, with further increasing the precursor concentration, although the light harvest spectrum of the QDs is broadened, nonetheless the PL intensity is reduced quickly (Figure 5 and Figure S3, Supporting Information). Therefore, the solar energy absorbed by the QDs is inefficiently converted due to the undesired defect states introduced during the growth of nanocrystals. Therefore, the device performances of solid-state QDSCs based on the optimized QDs were examined for five times (Figure 6d) and the photovoltaic parameters are summarized in **Table 1**. Under the identical experimental conditions, the QDSCs made from Nd_2Se_3 QDs exhibit the highest open-circuit voltage (V_{oc}) of 0.675 V and short-circuit current density (J_{sc}) of 8.30 mA cm^{-2}, thus demonstrating better performances than the other two types of solar cells, and achieve a decent PCE of 3.19%.

Notwithstanding, the three QDs exhibit similar band gap and the emission peak, now what is the driving force for such difference in the device performance? V_{OC} can be estimated according to the following relationship [37]

$$V_{OC} = |\mathrm{HOMO_D}| - |\mathrm{LUMO_A}| - \frac{kT}{q}\ln\left(\frac{N_{eff}^2}{np}\right) \quad (1)$$

where $HOMO_D$ is the highest occupied molecular orbital (HOMO) of the donor, $LUMO_A$ is the LUMO of the acceptor, k is the Boltzmann constant, q is the elementary charge, T is temperature, N_{eff} is the effective density of state, and n, p are the concentrations of electrons and holes, respectively. This relationship demonstrates that the V_{oc} is determined by the energy offset between $HOMO_D$ and $LUMO_A$. If the third term could be ignored, the more negative of C (i.e., HOMO) will give rise to a higher V_{oc}. In this sense, Nd_2Se_3 should have a higher value of V_{oc} than other two types of QDs and this is consistent with our measured results. Note that the photoexcited charge transfer at the interface is pertinent to the energy level formation between the donor and the acceptor. Moreover, it has been revealed that narrow energy difference between valence band (VB) of the donor (QDs herein) and the conduction band (CB) of the acceptor (TiO_2), i.e., E_{DA}, will suppress saturated dark current of the solar cells according to the relationship [9b]

$$J_0 = J_{00}\exp\left(-\frac{E_{DA}}{nkT}\right) \quad (2)$$

where k is the Boltzmann constant, T temperature, J_0 the saturated dark current density, J_{00} a factor for recombination of excitons (i.e., the bound electron–hole pairs), and n the diode ideality factor. As shown in Figure 8b and Table 3, the Nd_2Se_3/TiO_2 not only shows a largest value of E_{DA} than its counterparts,

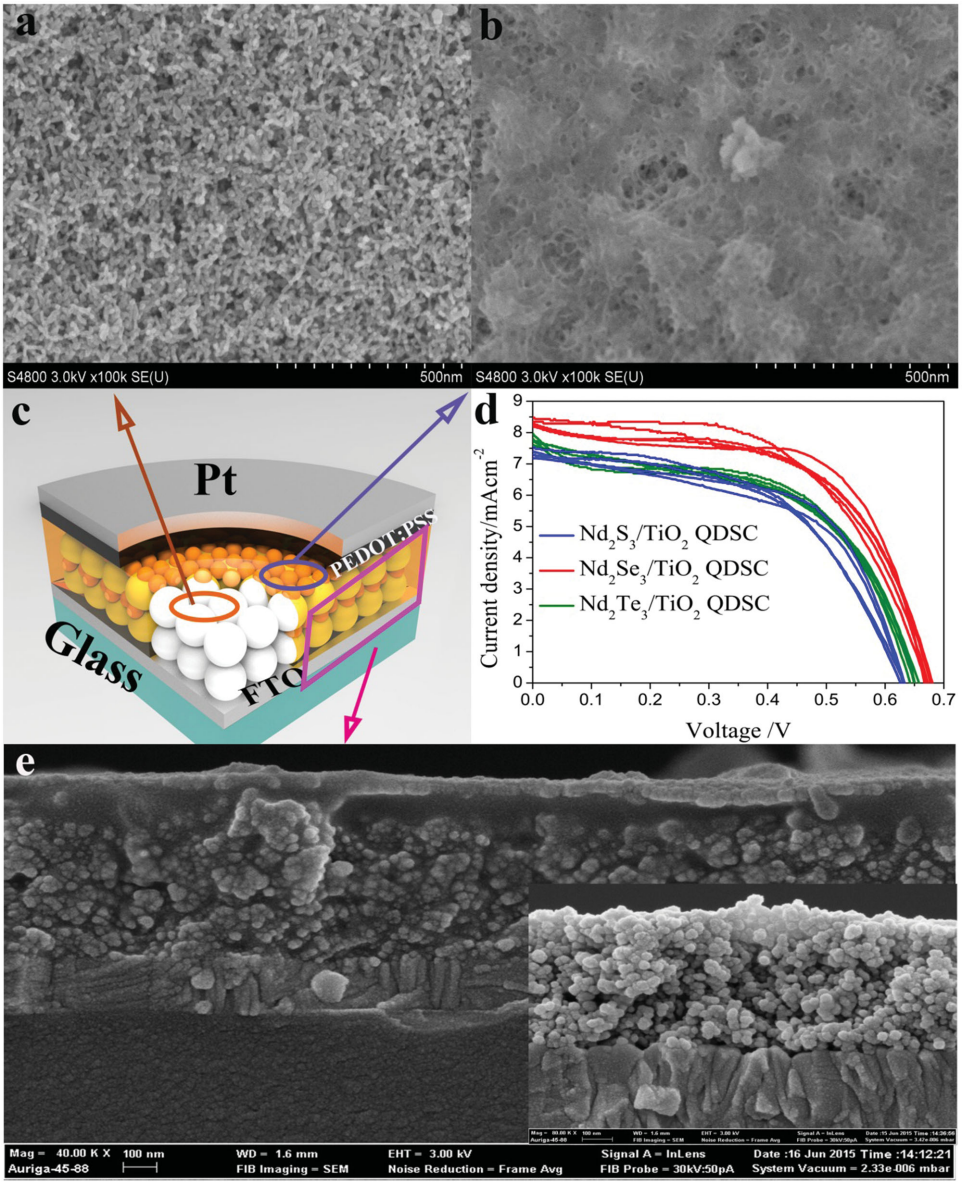

Figure 6. The morphologies and photovoltaic performances of nanostructured solid-state QDSCs. SEM images of a) pure TiO_2 and b) QDs/TiO_2 BHJ films, c) schematic diagram of the structure of QDSCs, d) photocurrent–voltage (*J–V*) characteristics of solid-state QDSCs made from TiO_2/Nd_2(S, Se, Te)$_3$ QDs, and e) Cross-sectional SEM image of QDs/TiO_2 BHJ. The insert highlights the cross-sectional SEM image of pure TiO_2 coated on FTO glass.

but also exhibits the longest PL lifetime (7199 ps) and fastest charge transfer rate (2.02×10^9 s^{-1}), all of which favor the photocurrent generation and suppress saturated dark current.

Table 1. Photoelectric properties of solid-state QDSCs based on different QDs.

BHJs	V_{oc} [V]	J_{sc} [mA cm^{-2}]	FF [%]	$\eta^{a)}$ [%]
Nd_2S_3/TiO_2	0.631 ± 0.004	7.32 ± 0.13	53.2 ± 0.9	2.46 ± 0.03
Nd_2Se_3/TiO_2	0.675 ± 0.006	8.30 ± 0.09	57.1 ± 1.1	3.19 ± 0.04
Nd_2Te_3/TiO_2	0.651 ± 0.005	7.71 ± 0.23	53.5 ± 1.1	2.68 ± 0.05

[a)] $\eta = J_{sc}\, V_{oc}\, FF/P_{in}$, where P_{in} = 100 mW cm^{-2} (AM 1.5).

Although it is not straightforward to explain the increase of J_{sc} from the viewpoint of optical characteristics, nonetheless the reduced electron–hole pair recombination, enhanced charge transfer rate together with narrower band gap can theoretically provide useful insight into the increased J_{sc}.

Next, the energy level diagram of Nd_2(S, Se, Te)$_3$ QDs/TiO_2 will be separately explored by the cyclic voltammetry (CV) characteristics,[38] Mott–Schottky method along with UV–vis absorption spectra[39] and UV photoelectron spectroscopy (UPS). CV is a promising and low-cost method to measure the absolute energy levels in semiconductor QDs, but is critically dependent on the medium where measurements are performed. Organic electrolyte such as tetrabutylammonium hexafluorophosphate ($TBAPF_6$) is preferred due to their broad potential window

available, which can provide very informative voltammograms about band edges and defect states for QDs.[16d,40] As observed from the CV characteristics in **Figure 7**a, both the oxidation and reduction waves of the $Nd_2(S, Se, Te)_3$ QD films are clearly revealed, implying that the films have the good capability to transport electrons and holes. All the electrochemical parameters are summarized in **Table 2**. Upon sweeping the films cathodically, the CB energy levels of the $Nd_2(S, Se, Te)_3$ QDs/TiO_2 films are individually estimated to be −3.71, −3.89, −3.86 eV, respectively. Meanwhile, upon anodic sweep, the VB energy levels corresponding to the peak potentials of $Nd_2(S, Se, Te)_3$ QDs/TiO_2 films are determined to be −5.99, −6.09, and −6.07 eV, respectively. The energy levels of HOMO (VB) and LUMO (CB edge) can be calculated using the following formula: HOMO (or LUMO) (eV) = $-4.8-(E-E_{1/2})$, where E is a peak point of the redox potential, $E_{1/2}$ is the ferrocene potential against Ag/Ag^+ system ($E_{1/2}$ vs Ag/Ag^+ = 0.09 eV), which should be measured in the electrolyte solution using the same reference electrode, and −4.80 eV is the energy level in the vacuum.

Besides, Mott–Schottky plots together with UV–vis absorption spectra are used to separately estimate the CB and VB energy levels of the QDs films as shown in Figure 7b,c, respectively. The electrochemical parameters including CB, VB, band gap determined by CV and Mott–Schottky method along with UV–vis absorption spectra are listed in Table 2. It can be observed that the results obtained from the UV–vis absorption spectra and Mott–Schottky method are in reasonable agreement with those determined from the CV characteristics, indicating that our experiments are performed on a reliable and comparable basis. The energy offsets between the CB energy level of $Nd_2(S, Se, Te)_3$ QDs and LUMO of TiO_2 as shown in Figure 7d are 0.41, 0.31, and 0.34 eV, respectively. The results show that the relative positions of both VB and CB have changed as compared with pure TiO_2, which are important for the intended desired charge transfer of BHJs and are discussed

Table 2. Electrochemical parameters of the $Nd_2(S, Se, Te)_3$ QDs/TiO_2 films.

Films	E_{red} [a)] [V]/CB[eV]	E_{OX} [a)] [V]/VB[eV])	E_g [a)] [eV]	Flat-band potential[V]/CB[b)] [eV]	E_g [b)] [eV]	VB[b)] [V]
Nd_2S_3	−1.00/−3.71	1.28/−5.99	2.28	−0.90/−3.81	2.41	−6.22
Nd_2Se_3	−0.82/−3.89	1.38/−6.09	2.20	−0.73/−3.98	2.32	−6.30
Nd_2Te_3	−0.85/−3.86	1.36/−6.07	2.21	−0.76/−3.95	2.39	−6.34

[a)]Electrochemical parameters were obtained from CVs. The band gap was calculated from the difference between VB and CB values; [b)]The CB values were determined by Mott–Schottky plots and the band gap was estimated from the UV–vis spectrum, then the VB values were derived from the difference between CB and band gap values.

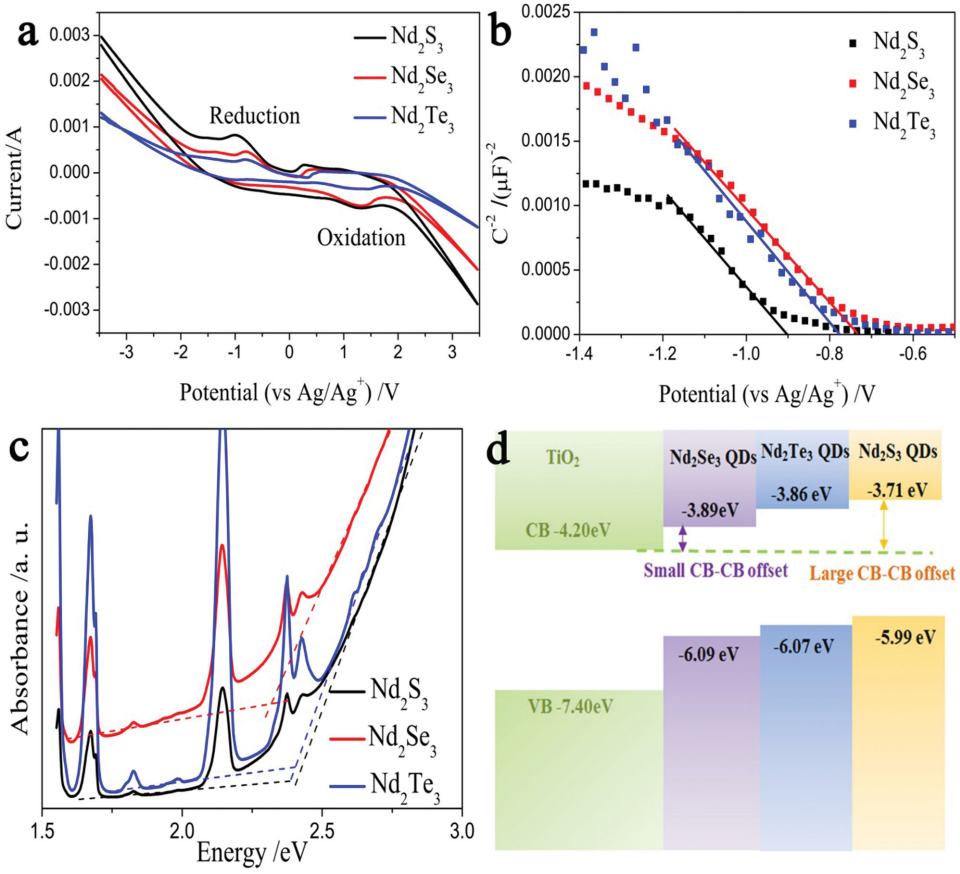

Figure 7. The energy band of $Nd_2(S, Se, Te)_3$ QDs. a) CV characteristics, b) Mott–Schottky curves, c) UV–vis absorption spectra, and d) energy level diagram of $Nd_2(S, Se, Te)_3$ QDs.

below. Among the three types of QDs, Nd_2Se_3 QDs have the smallest band gap and CB-LUMO energy offset.

Apart from the electrochemical methods, UPS was applied to separately explore the occupied electronic states of the QDs for comparison, thus allowing one to obtain the value of Fermi level and the VB level from the low-binding energy cutoff and energy cutoff, respectively.[32b,40,41] The full UPS spectra and the energy differences are shown in **Figure 8**a, from which both Fermi level (E_f) and VB with respect to the vacuum level are derived. Figure 8c,d displays the enlarged views of the cutoff regions, respectively, and the onset values are determined from the intersection of a linear extrapolation from the cutoff region to the baseline. **Table 3** summarizes the energies of the VB, Fermi level, and CB levels that are determined by CB = VB + E_g (E_g is the optical bandgap). The Nd_2Se_3 QDs reveal a deeper VB level, i.e., –6.40 eV as compared to Nd_2S_3 and Nd_2Te_3 QDs. The band gap was determined from the UV–vis absorption spectrum (Figure 4a) using the following relationship: $E_g = 1240/\lambda$ eV, where λ is the onset absorption wavelength.

Next, we will demonstrate that the reduction of the 'excess energy' offset at donor/acceptor indeed enables more energetic electron transfer to the interface and leads to better charge collection and correspondingly higher current density.[13,42] The comparative studies of $Nd_2(S, Se, Te)_3$ QD neat films against $Nd_2(S, Se, Te)_3$ QDs/TiO_2 blend films enable the identification of the role of QDs in the electron transfer at the BHJ interfaces. The time-resolved single-photon counting PL decays are shown in **Figure 9**a–c. Laser excitation of $Nd_2(S, Se, Te)_3$ QDs that were absorbed on TiO_2 results in electron(e)–hole (h) separation (reaction 1), followed by either recombination of the charge carriers (reaction 2) or an additional deactivation pathway for the bleaching recovery, in which photogenerated electrons are injected into the TiO_2 nanoparticles (reaction 3)

$$Nd_2(S,Se,Te)_3 + h\nu \rightarrow Nd_2(S,Se,Te)_3(h+e) \quad \text{(reaction 1)}$$

$$Nd_2(S,Se,Te)_3(h+e) \rightarrow Nd_2(S,Se,Te)_3 + h\nu' \quad \text{(reaction 2)}$$

$$Nd_2(S,Se,Te)_3(e) + TiO_2 \rightarrow Nd_2(S,Se,Te)_3 + TiO_2(e) \quad \text{(reaction 3)}$$

The bleaching revovery occurs with a range of heterogeneous kinetics but can be fitted to a sum of two-exponential function

Table 3. Energy-cutoff values from UPS measurements and the energy level values with respect to vacuum level.

QDs	$E_{fcutoff}$ [eV]	$VB_{cuttoff}$ [eV]	E_f [eV]	VB [eV]
Nd_2S_3	15.89	0.58	–5.33	–5.91
Nd_2Se_3	15.72	0.90	–5.50	–6.40
Nd_2Te_3	15.85	0.72	–5.37	–6.09

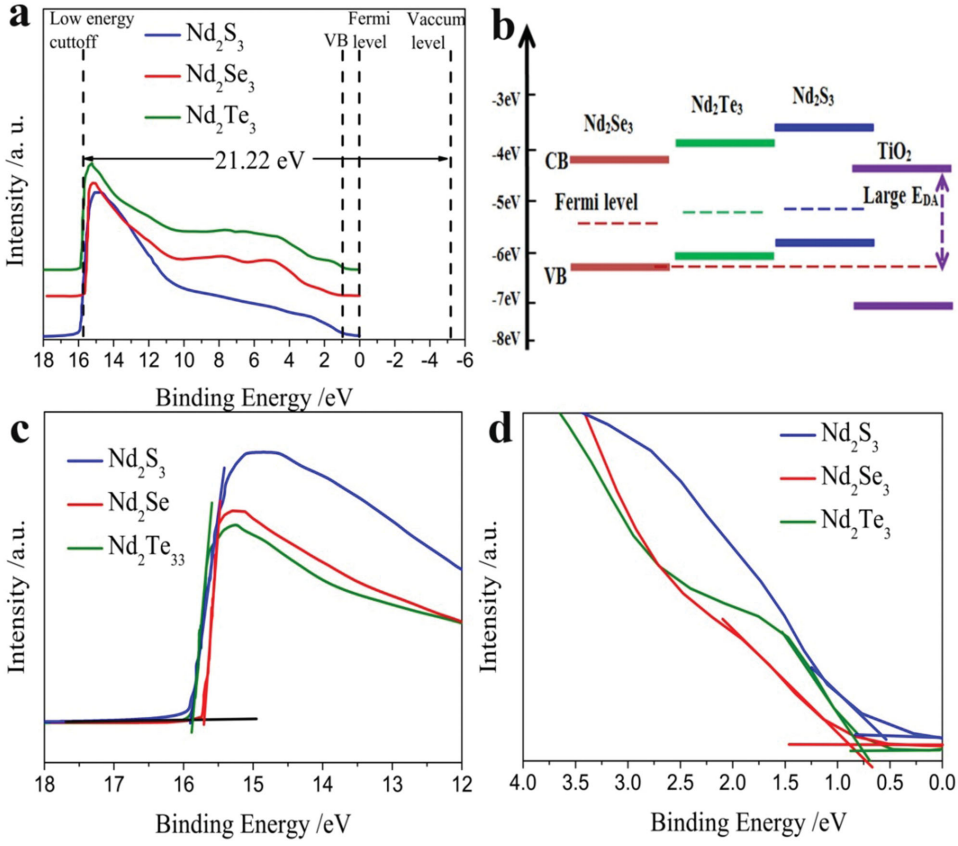

Figure 8. a) Full UPS spectra of Nd_2S_3, Nd_2Se_3, and Nd_2Te_3 QDs, b) energy level diagram of the QDs, c) magnified views of the low-binding-energy cutoff, and d) high-binding -energy cutoff regions.

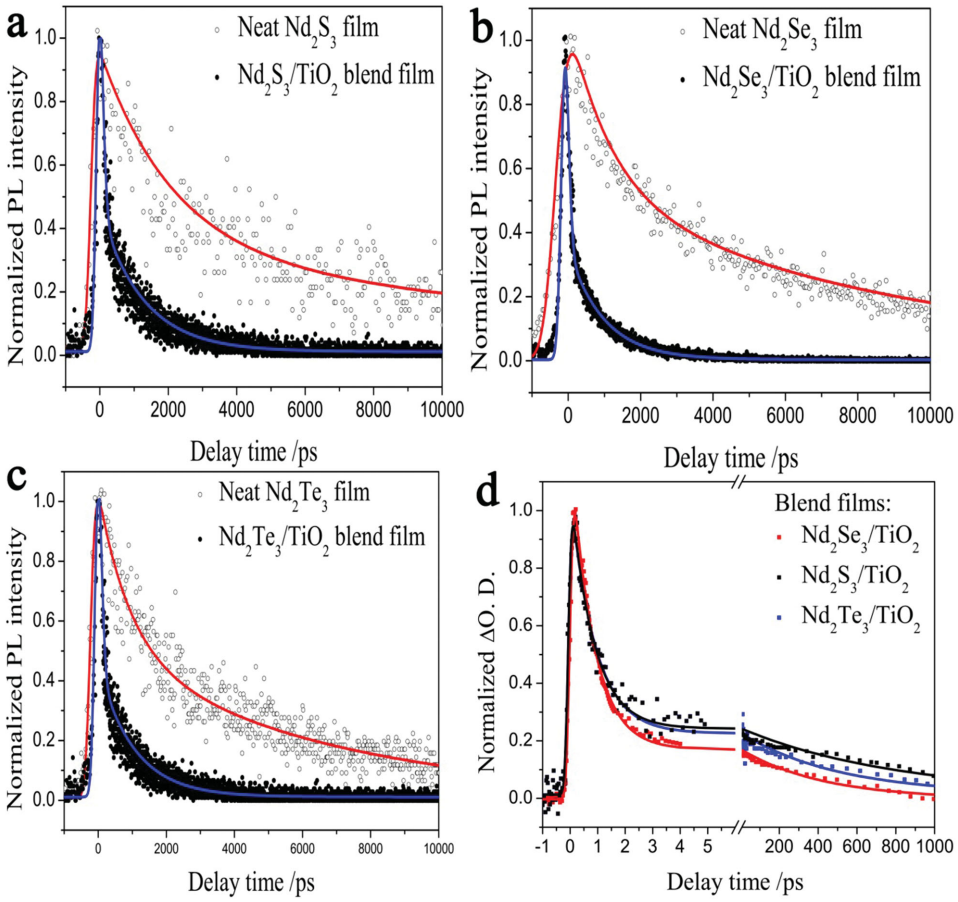

Figure 9. a–c) Normalized femtosecond transient absorption decays of pure $Nd_2(S, Se, Te)_3$ QD neat films (open circle) and $Nd_2(S, Se, Te)_3$ QD/TiO_2 blend films (solid circle), and d) highlights comparative plots of normalized femtosecond transient absorption (TA) decays of the three blend films.

(Equation (3)), which was found to be satisfactory in determination of emission lifetimes

$$I(t) = [a_1 \exp(-t/\tau_1) + a_2 \exp(-t/\tau_2)] \otimes F(t) \quad (3)$$

where $F(t)$ is the impulse response function (IRF), a is the amplitude, and τ is the time constant. $F(t)$ is related with half width at half-maximum (HWHM) of the pulse duration and then fitted to the data points in order to numerically simulate the measured fluorescence dynamics. These values were then used to estimate the average lifetime $\langle\tau\rangle$ of $Nd_2(S, Se, Te)_3$ emission decay using Eq. (4)

$$\langle\tau\rangle = \frac{a_1\tau_1^2 + a_2\tau_2^2}{a_1\tau_1 + a_1\tau_2} \quad (4)$$

The electron transfer (or injection) rate constant can be obtained from Eq. (5) as follows

$$k_{et} = \frac{1}{\tau_{Nd_2(S,Se,Te)_3/TiO_2}} - \frac{1}{\tau_{Nd_2(S,Se,Te)_3}} \quad (5)$$

The average fluorescence life times $\langle\tau\rangle$ of the different neat QD films are individually determined to be 5.7, 7.2, and 6.3 ns for $Nd_2(S, Se, Te)_3$ QDs, respectively, as shown in **Table 4**. After QDs were incorporated into and interfaced with the electron extraction TiO_2 layer, the PL emission is greatly quenched after about 500 ps and the PL lifetimes were substantially shortened, indicating that there exists a strong photoexcited charge carrier transfer at the interface of the BHJs. And the fitted PL lifetimes $\tau_{heterojuction}$ (i.e., $\tau_{Nd2(S,Se,\ Te)\ +\ TiO2}$) were determined to be 821, 495, and 751 ps for Nd_2S_3/TiO_2, Nd_2Se_3/TiO_2, and Nd_2Te_3/TiO_2, respectively. Correspondingly, according to the Eq. (5), the charge transfer rate k_{ct} can be estimated to be 1.22, 2.02, and 1.33×10^9 s^{-1} for Nd_2S_3/TiO_2, Nd_2Se_3/TiO_2, and Nd_2Te_3/TiO_2 BHJs, respectively, indicating that much faster charge carrier transfer occurs at the Nd_2Se_3/TiO_2 interface than Nd_2S_3/TiO_2 and Nd_2Te_3/TiO_2 interfaces.

In order to further enquire into the photoexcited charge transfer dynamics and electron injection rate from QDs to TiO_2 substrate, the femtosecond transient absorption spectroscopy was applied to investigate the electron injection and recombination dynamics. As shown in Figure 9d, the positive singal probed at 570 nm is ascribed to the photoinduced excited state absorptions (PA) originating from the so-called state-filling effects.[43] analysis of the PA transients would provide detailed insight into the photoexcited electron dynamics. It can be observed that all the films exhibit a prominent symmetrical peak near zero

Table 4. Kinetic parameters obtained from fits to time-resolved PL and TA decays.

Kinetic parameters	a_1	a_2	τ_1 [ps]	τ_2 [ps]	$\langle\tau\rangle$ [ps]	k_{et} [a)] [$\times 10^9$ s^{-1}]	k_{et} [b)] [$\times 10^9$ s^{-1}]
Nd_2S_3	0.64	0.51	970 ± 80	6555 ± 226	5680	1.22	1.25
Nd_2S_3/TiO_2	0.77	0.42	267 ± 24	1074 ± 108	821		
Nd_2Se_3	0.67	0.57	950 ± 107	8078 ± 292	7199	2.02	2.50
Nd_2Se_3/TiO_2	0.85	0.23	149 ± 8	750 ± 13	495		
Nd_2Te_3	0.58	0.39	1205 ± 276	7500 ± 386	6286	1.33	2.00
Nd_2Te_3/TiO_2	0.60	0.37	411 ± 25	982 ± 65	751		

[a)] k_{et} is obtained from time-resolved PL results while; [b)] k_{et} is derived from the TA decays of the BHJs by using Equation (8).

delay, which is assigned to the prominent contributions from the electronic hyperpolarizability. Subsequently, a fast decay with decay time τ_{vib} that originates from the vibronic relaxations of the QDs is clearly shown in the time domain ≈1–5 ps. Finally, a long tail dominates the contribution in long time delay, which can be ascribed to the charge transfer at the interface. Therefore, we decompose the PA signals of these films into three dynamically distinct components. All these transients were fitted with a biexponential function (Supporting Information),[44] and the fitted constants were sumarized in Table S3 in the Supporting Information. Using the lifetime values, electron-transfer rates were calculated using Equation (5) and listed in Table 3. We found that the charge transfer rates k_{ct} are 1.25, 2.50, and 2.00 × 10^9 s^{-1} for Nd_2S_3, Nd_2Se_3, and Nd_2Te_3 QD BHJs, respectively, which are in reasonable agreement with the time-resolved PL results. Consequently, Nd_2Se_3/TiO_2 BHJ with the smallest but still large enough CB–CB offset to break the Coulomb attraction (typically ≈0.1–0.5 eV) leads to the fastest charge transfer. The reduction of the 'excess' energy offset should be responsible for the shorter electron transfer lifetime at the interface of BHJ. The orgin of the decrease in the transfer lifetime with reducing the energy offset can be explained by the fact that the energy offset is located in Marcus "inverted" region,[45] in which the electron transfer becomes much faster due to the decreased energy offset.[8b] Since hole extraction from QD to the PEDOT:PSS layer should be equally important to the electron transfer from the QD to TiO_2, here time-integrated PL spectra were carried out to explore the electron and hole transfer at the interface (Figure S7, Supporting Information). The PL intensities are greatly reduced in both TiO_2/QDs and QDs/PEDOT:PSS blend films as compared with pure QDs. This suggests that a higher degree of the photo-induced electron/hole transfer has occurred in the BHJs.

3. Conclusion

We have successfully prepared the Nd-VI QD sensitizers for the first time, i.e., Nd_2(S, Se, Te)$_3$ QDs, as a lighter absorber via solution-processed method, and their optical and photophysical properties were studied by spectroscopic and photoelectrochemical techniques. The composition and chemical status of the synthesized QDs have been analyzed using ICP-AES together with EDS and XPS, respectively. The sizes of the QDs were controlled by varying the ratios of Nd to chalcogenide precursors (e.g., S, Se, Te) and the optimum ratios were obtained by exploring the optical properties. The results show that both the absorption band and the emission band have been redshifted, thus leading to an improvement in light harvesting, and Nd_2S_3, Nd_2Se_3, and Nd_2Te_3 QDs exhibit the most significant redshift simultaneously without completely sacrificing PL intensity at the molar ratio of 1:0.675, 1:0.65, and 1: 0.275, respectively. The averaged diameters of the as-prepared QDs at the optimum ratios are 2.9, 5.9, and 4.2 nm for Nd_2S_3, Nd_2Se_3, and Nd_2Te_3 QDs, respectively. The energy level diagram of the QDs was separately examined using UPS, CVs, and Mott–Schottky method together with UV–vis absorption spectra, indicating that Nd_2Se_3 QDs present much smaller energy offset between the CB energy level and LUMO of TiO_2 (0.31 eV only) than Nd_2S_3 and Nd_2Te_3 QDs do. Consequently, the electron transfer lifetime of Nd_2Se_3 QDs (≈0.5 ns) becomes much faster than those of Nd_2S_3 and Nd_2Te_3 QDs. The potential of the wide adsorption QDs in photovoltaics was demonstrated by engineering novel rare-earth chalcogenide QDs and a decent PCE of 3.19% was achieved for Nd_2Se_3 QDs.

4. Experimental Section

Materials: Chemical reagents including tetrabutyl titanate, polyethylene glycol (PEG, molecular weight of 20 000), P25(Degussa), nitric acid, acetic acid, acetone, octyl polyethylene (OP) emulsifying agent (Triton X-100), neodymium nitrate hexahydrate, glutathione (GSH), isopropanol, sodium borohydride, sodium sulfide, selenium, tellurium, absolute ethanol are analytic purity and purchased from Sigma-Aldrich Ltd., Hongkong, China. The PEDOT: PSS was provided by Aldrich. FTO glass (sheet resistance 8 Ω cm^{-2}) was purchased from Hartford Glass Co., USA.

Preparation of n-Type-TiO2 Colloid: TiO_2 colloid was prepared by the procedures in a similar way as done in the previous works.[38b,39b] Briefly, tetrabutyl titanate (10 mL) was added to distilled water (100 mL) under stirring, followed by a white precipitate immediately. The precipitate was filtered, washed with distilled water, and then transferred to a mixed solution (150 mL) containing nitric acid (1 mL) and acetic acid (10 mL) at 80 °C. Finally, the mixture was hydrothermally treated in an autoclave at 200 °C for 24 h to form a colloid of TiO_2. Subsequently, the P25 (0.075 g) were added in TiO_2 colloid by repeating crystallization at 200 °C for 12 h. At last, the resultant slurry was concentrated by a thermal evaporation and PEG-20000 (0.5 g) and a few drops of the Triton X-100 emulsification reagent were added and an even and stable n-type TiO_2 colloid was produced.

Preparation of S, Se, and Te Precursors: As for the Se precursor, a mixture of selenium powder (0.1 g) and absolute ethanol (20 mL) was prepared at room temperature. Subsequently, sodium borohydride (0.12 g) was quickly injected to the mixed solution under nitrogen atmosphere and under vigorous stirring a colorless Se precursor was formed; as for the preparation of Te precursor, tellurium (0.05 g) was dissolved into deionized water (25 mL) at room temperature, followed by quickly injecting sodium borohydride (0.25 g) into the mixed solution, and after vigorous stirring under nitrogen atmosphere, the colorless Te precursor was formed (NaHTe that exists in the form of HTe^-); as for the preparation of S precursor, sodium sulfide (1.95 g) was completely dissolved into deionized water (250 mL) at room temperature under N_2 atmosphere and then under vigorous stirring, the colorless S precursor was formed.

Preparation of GSH-modified Nd_2(S, Se, Te)$_3$ QDs: A series of aqueous colloidal Nd_2(S, Se, Te)$_3$ QDs were prepared in the presence of GSH as stabilizing agent.[46] Briefly, 0.1 M neodymium nitrate hexahydrate

(25 mL) acting as Nd precursor was firstly diluted to 100 mL in a three-necked flask in the presence of GSH (60 μL), then the pH of the solution was adjusted to 3 by adding a few drops of 0.5 M HNO_3, followed by being degassed at 100 °C for 1 h. Then, the solution was heated to 100 °C under nitrogen atmosphere for 20 min. After that, an appropriate and varied amount of S, Se, or Te precursor was rapidly injected into the hot solution, respectively, under vigorous stirring for 1 h and then $Nd_2(S, Se, Te)_3$ colloidal QDs were formed. Finally, the mixture was hydrothermally treated at 200 °C for 12 h in an autoclave, followed by being purified by precipitation twice in absolute alcohol and acetone, and dried under nitrogen flow and stored in solid form in a nitrogen-filled glove box.

Device Fabrication: A layer of n-type TiO_2 film with a thickness of 250 nm was prepared by coating the TiO_2 colloid on FTO glass using a spin-coated technique, followed by sintering in air at 450 °C for 30 min. Then, the acceptor film was soaked in a 25 mg mL^{-1} GSH-modified $Nd_2(S, Se, Te)_3$ QDs aqueous solution (identical concentration for all the three types of QDs and QDs with different sizes) for 12 h to uptake p-type QDs and dried under nitrogen flow. Next, PEDOT:PSS layer was spin-coated onto the BHJ. Finally, Pt electrodes were deposited on the top of the PEDOT:PSS layer by thermal evaporation under vacuum.

Characterizations: The microstructures of the $Nd_2(S, Se, Te)_3$ QDs were characterized by means of HR-TEM (JEM-2010, JEOL Ltd.) working at 200 kV. Samples for HR-TEM were prepared by ultrasonically dispersing the samples, placing a small volume of this suspension on carbon-enhanced copper grids, and drying in air. The morphologies of the TiO_2 acceptor layer and the cross-section of QDs/TiO_2 BHJ were characterized by a field emission SEM (FE-SEM, Hitachi S4800). The composition of the prepared QDs was monitored by ICP-AES, LeemanCo., USA, PROFILE SPEC and EDS. The crystalline structures of the samples were characterized by XRD patterns on a X-ray diffractometer (MiniFlex II, Rigaku Ltd., Japan) using Cu Kα radiation (λ = 0.154 nm) at 50 kV and 250 mA at room temperature. The PL spectrum was measured by using a spectrophotometer (FLS920, Edinburgh), in which a xenon lamp and a photomultiplier tube (R955, Hamamatsu) were used as excitation source and fluorescence detector. UV–vis absorption spectra were recorded with a Varian Cary 300 spectrophotometer. The CV results were obtained using a BAS (Bioanalytical Systems, Inc.) 100B instrument (BASi Inc., USA) at room temperature and at a scan rate of 100 mV s^{-1}. The Ag/Ag^+ (0.01 M of $AgNO_3$ + 0.1 M $TBAPF_6$ in acetonitrile as supporting electrolyte), a platinized platinum (1.0 cm^2) and QDs-coated platinum were used as reference electrode, counter electrode, and working electrode, respectively. The three electrodes were immersed in 0.1 M $TBAPF_6$ acetonitrile solution in a cell under nitrogen protection. The Mott–Schottky measurements were performed at the frequency of 1 kHz in the aqueous solution of 0.05 M Na_2SO_4 using a BAS 100B instrument and Ag/Ag^+ electrode as the reference electrode. The UPS spectra measurements were performed at room temperature in an ultrahigh vacuum photoelectron spectrometer ESCALAB 250Xi Ver 2 electron energy spectrometer with He–I radiation ($h\nu$ = 21.22 eV) as UV source. The chamber pressure was kept within 2×10^{-8} Pa during the UPS measurements. The QDs were spin-coated on to a gold substrate for UPS measurements. The *J–V* curves of the assembled QDSCs were recorded on an Electrochemical Workstation (Xe Lamp Oriel Sol3A Class AAA Solar Simulators 94023A, USA) under an irradiation of a simulated solar light from a 100 W xenon arc lamp in ambient atmosphere. The sweep speed of the *J–V* measurements is 0.5 mV s^{-1}.

Electron-Transfer Dynamics Measurement: Charge photogeneration dynamics of the BHJs were measured by the mode-locked Ti:sapphire laser (Coherent Mira 900) in combination with a regenerative amplifier (Coherent Legend-F). Time-resolved photoluminescence was measured on a spectrometer (Bruker Optics 250IS/SM) with intensified charge coupled device (CCD) detector (Andor, IStar740). The ultrafast light source with a temporal resolution of ≈120 fs was generated by a mode-locked titanium–sapphire laser operating at 800 nm. An optical parametric amplifier (OPA-800CF-1, Spectra Physics) provided ultrashort laser pulses at desired wavelengths (≈120 fs, full width at half maximum). A continuum white light generated from a sapphire plate was directed into the excited sample and detected by a CCD detector. Ultrashort laser pulses at 400 nm were employed as the pump light for the sample excitation and the probe light for the absorption measurement. Transient absorption at various delay times could be measured by controlling the arrival time of each laser pulse at the sample. The laser system was operated at a repetition rate of 10 Hz, thus each pulse excited fully relaxed sample. Each data was obtained by averaging 100 individual measurements to improve the signal-to-noise ratio, and the typical detection sensitivity of the difference absorption (ΔOD) was better than 10^{-4}.

Supporting Information

Supporting Information is available from the Wiley Online Library or from the author.

Acknowledgements

The authors gratefully acknowledge the financial support of the Natural Science Foundation of China (Grant Nos. 11564026 and 61366003), the science and technology project of the education department of Jiangxi Province, China (Grant Nos. GJJ13474 and GJJ14533), and the Natural Science Foundation of Jiangxi Province (Grant No. 20142BAB213015).

Received: August 14, 2015
Revised: September 18, 2015
Published online: November 30, 2015

[1] C. D. M. Donega, *Chem. Soc. Rev.* **2011**, *40*, 1512.
[2] a) L. Sun, J. J. Choi, D. Stachnik, A. C. Bartnik, B.-R. Hyun, G. G. Malliaras, T. Hanrath, F. W. Wise, *Nat. Nanotechnol.* **2012**, *7*, 369; b) M. A. Baldo, D. F. O'Brien, Y. You, A. Shoustikov, S. Sibley, M. E. Thompson, S. R. Forrest, *Nature* **1998**, *395*, 151; c) B. S. Mashford, M. Stevenson, Z. Popovic, C. Hamilton, Z. Zhou, C. Breen, J. Steckel, V. Bulovic, M. Bawendi, S. Coe-Sullivan, P. T. Kazlas, *Nat. Photon.* **2013**, *7*, 407.
[3] M. Law, H. Kind, B. Messer, F. Kim, P. Yang, *Angew. Chem. Int. Edit.* **2002**, *41*, 2405.
[4] a) U. Resch-Genger, M. Grabolle, S. Cavaliere-Jaricot, R. Nitschke, T. Nann, *Nat. Methods* **2008**, *5*, 763; b) W. C. Law, K. T. Yong, I. Roy, H. Ding, R. Hu, W. Zhao, P. N. Prasad, *Small* **2009**, *5*, 1302.
[5] a) J. Gao, J. M. Luther, O. E. Semonin, R. J. Ellingson, A. J. Nozik, M. C. Beard, *Nano Lett.* **2011**, *11*, 1002; b) P. K. Santra, P. V. Kamat, *J. Am. Chem. Soc.* **2013**, *135*, 877; c) S. Kim, M. Kang, S. Kim, J.-H. Heo, J. H. Noh, S. H. Im, S. I. Seok, S.-W. Kim, *ACS Nano* **2013**, *7*, 4756; d) Z. Pan, H. Zhang, K. Cheng, Y. Hou, J. Hua, X. Zhong, *ACS Nano* **2012**, *6*, 3982; e) Z. Ning, D. Zhitomirsky, V. Adinolfi, B. Sutherland, J. Xu, O. Voznyy, P. Maraghechi, X. Lan, S. Hoogland, Y. Ren, E. H. Sargent, *Adv. Mater.* **2013**, *25*, 1719; f) M. Yuan, D. Zhitomirsky, V. Adinolfi, O. Voznyy, K. W. Kemp, Z. Ning, X. Lan, J. Xu, J. Y. Kim, H. Dong, E. H. Sargent, *Adv. Mater.* **2013**, *25*, 5586; g) C.-H. M. Chuang, P. R. Brown, V. Bulović, M. G. Bawendi, *Nat. Mater.* **2014**, *13*, 796; h) A. J. Labelle, S. M. Thon, S. Masala, M. M. Adachi, H. Dong, M. Farahani, A. H. Ip, A. Fratalocchi, E. H. Sargent, *Nano Lett.* **2015**, *15*, 1101; i) G. H. Carey, L. Levina, R. Comin, O. Voznyy, E. H. Sargent, *Adv. Mater.* **2015**, *27*, 3325; j) I. J. Kramer, J. C. Minor, G. Moreno-Bautista, L. Rollny, P. Kanjanaboos, D. Kopilovic, S. M. Thon, G. H. Carey, K. W. Chou, D. Zhitomirsky, A. Amassian, E. H. Sargent, *Adv. Mater.* **2015**, *27*, 116.
[6] F. Marlow, A. Hullermann, L. Messmer, *Adv. Mater.* **2015**, *27*, 2447.
[7] B. R. Sutherland, S. Hoogland, M. M. Adachi, P. Kanjanaboos, C. T. O. Wong, J. J. McDowell, J. Xu, O. Voznyy, Z. Ning, A. J. Houtepen, E. H. Sargent, *Adv. Mater.* **2015**, *27*, 53.

[8] a) Y. Liang, Z. Xu, J. Xia, S. T. Tsai, Y. Wu, G. Li, C. Ray, L. Yu, *Adv. Mater.* **2010**, *22*, E135; b) X. Gong, M. Tong, F. G. Brunetti, J. Seo, Y. Sun, D. Moses, F. Wudl, A. J. Heeger, *Adv. Mater.* **2011**, *23*, 2272; c) H. Yu, H. Irie, K. Hashimoto, *J. Am. Chem. Soc.* **2010**, *132*, 6898.
[9] a) W. Li, W. S. C. Roelofs, M. M. Wienk, R. A. J. Janssen, *J. Am. Chem. Soc.* **2012**, *134*, 13787; b) B. Yang, Y. Yuan, P. Sharma, S. Poddar, R. Korlacki, S. Ducharme, A. Gruverman, R. Saraf, J. Huang, *Adv. Mater.* **2012**, *24*, 1455; c) L. Dou, J. You, J. Yang, C.-C. Chen, Y. He, S. Murase, T. Moriarty, K. Emery, G. Li, Y. Yang, *Nat. Photon.* **2012**, *6*, 180; d) A. Luque, A. Marti, C. Stanley, *Nat. Photon.* **2012**, *6*, 146; e) A. H. Ip, S. M. Thon, S. Hoogland, O. Voznyy, D. Zhitomirsky, R. Debnath, L. Levina, L. R. Rollny, G. H. Carey, A. Fischer, K. W. Kemp, I. J. Kramer, Z. Ning, A. J. Labelle, K. W. Chou, A. Amassian, E. H. Sargent, *Nat. Nanotechnol.* **2012**, *7*, 577.
[10] a) I. J. Kramer, E. H. Sargent, *ACS Nano* **2011**, *5*, 8506; b) L. Etgar, T. Moehl, S. Gabriel, S. G. Hickey, A. Eychmüller, M. Grätzel, *ACS Nano* **2012**, *6*, 3092.
[11] a) N. M. Gabor, J. C. W. Song, Q. Ma, N. L. Nair, T. Taychatanapat, K. Watanabe, T. Taniguchi, L. S. Levitov, P. Jarillo-Herrero, *Science* **2011**, *334*, 648; b) K. J. Tielrooij, J. C. W. Song, S. A. Jensen, A. Centeno, A. Pesquera, A. Zurutuza Elorza, M. Bonn, L. S. Levitov, F. H. L. Koppens, *Nat. Phys.* **2013**, *9*, 248.
[12] a) L. W. Barbour, M. Hegadorn, J. B. Asbury, *J. Am. Chem. Soc.* **2007**, *129*, 15884; b) J. Guo, H. Ohkita, H. Benten, S. Ito, *J. Am. Chem. Soc.* **2010**, *132*, 6154; c) R. A. Marsh, J. M. Hodgkiss, S. Albert-Seifried, R. H. Friend, *Nano Lett.* **2010**, *10*, 923.
[13] S. A. McDonald, G. Konstantatos, S. Zhang, P. W. Cyr, E. J. Klem, L. Levina, E. H. Sargent, *Nat. Mater.* **2005**, *4*, 138.
[14] a) E. H. Sargent, *Nat. Photon.* **2012**, *6*, 133; b) I. J. Kramer, E. H. Sargent, *Chem. Rev.* **2014**, *114*, 863.
[15] a) D. Zhitomirsky, O. Voznyy, S. Hoogland, E. H. Sargent, *ACS Nano* **2013**, *7*, 5282; b) H. C. Leventis, F. O'Mahony, J. Akhtar, M. Afzaal, P. O'Brien, S. A. Haque, *J. Am. Chem. Soc.* **2010**, *132*, 2743.
[16] a) X. Peng, L. Manna, W. Yang, J. Wickham, E. Scher, A. Kadavanich, A. P. Alivisatos, *Nature* **2000**, *404*, 59; b) C. Y. Chen, C. T. Cheng, C. W. Lai, Y. H. Hu, P. T. Chou, Y. H. Chou, H. T. Chiu, *Small* **2005**, *1*, 1215; c) Y. Wang, S. Li, S. V. Kershaw, F. Hetsch, A. Y. Tam, G. Shan, A. S. Susha, C. C. Ko, V. Wing-Wah Yam, K. K. Lo, A. L. Rogach, *ChemPhysChem* **2012**, *13*, 2589; d) Y. C. Li, H. Z. Zhong, R. Li, Y. Zhou, C. H. Yang, Y. F. Li, *Adv. Funt. Mater.* **2006**, *16*, 1705.
[17] a) O. E. Semonin, J. M. Luther, S. Choi, H. Y. Chen, J. Gao, A. J. Nozik, M. C. Beard, *Science* **2011**, *334*, 1530; b) L. Sun, Z. Y. Koh, Q. Wang, *Adv. Mater.* **2013**, *25*, 4598; c) W. A. Tisdale, K. J. Williams, B. A. Timp, D. J. Norris, E. S. Aydil, X. Y. Zhu, *Science* **2010**, *328*, 1543.
[18] Y.-P. Sun, B. Zhou, Y. Lin, W. Wang, K. A. S. Fernando, P. Pathak, M. J. Meziani, B. A. Harruff, X. Wang, H. Wang, P. G. Luo, H. Yang, M. E. Kose, B. Chen, L. M. Veca, S.-Y. Xie, *J. Am. Chem. Soc.* **2006**, *128*, 7756.
[19] J. H. Warner, A. Hoshino, K. Yamamoto, R. D. Tilley, *Angew. Chem. Int. Edit.* **2005**, *44*, 4550.
[20] a) H. Zhang, Z. Cui, Y. Wang, K. Zhang, X. Ji, C. Lü, B. Yang, M. Gao, *Adv. Mater.* **2003**, *15*, 777; b) H. Zhang, Z. Zhou, B. Yang, M. Gao, *J. Phys. Chem. B* **2002**, *107*, 8.
[21] B. Vijaya Kumar, R. Velchuri, G. Prasad, B. Sreedhar, K. Ravikumar, M. Vithal, *Ceram. Int.* **2010**, *36*, 1347.
[22] T. Toliński, A. Kowalczyk, G. Chełkowska, *Phys. Lett. A* **2003**, *308*, 75.
[23] V. Bilovol, S. Ferrari, D. Derewnicka, F. D. Saccone, *Mater. Chem. Phys.* **2014**, *146*, 269.
[24] A. Stavrinadis, A. K. Rath, F. P. de Arquer, S. L. Diedenhofen, C. Magen, L. Martinez, D. So, G. Konstantatos, *Nat. Commun.* **2013**, *4*, 2981.
[25] B. Ehrler, B. J. Walker, M. L. Böhm, M. W. B. Wilson, Y. Vaynzof, R. H. Friend, N. C. Greenham, *Nat. Commun.* **2012**, *3*, 1019.
[26] A. Meerschaut, J. Rouxel, *Crystal Chemistry and Properties of Materials with Quasi-One-Dimensional Structures*, Vol. *5* (Ed: J. Rouxel), Springer, Netherlands, **1986**.
[27] B. Ehrler, B. J. Walker, M. L. Bohm, M. W. Wilson, Y. Vaynzof, R. H. Friend, N. C. Greenham, *Nat. Commun.* **2012**, *3*, 1019.
[28] a) Z. Liu, Y. Sun, J. Yuan, H. Wei, X. Huang, L. Han, W. Wang, H. Wang, W. Ma, *Adv. Mater.* **2013**, *25*, 5772; b) A. Panneerselvam, M. Green, *Nanoscience* **2012**, *1*, 208; c) J. E. Riggs, Z. Guo, D. L. Carroll, Y.-P. Sun, *J. Am. Chem. Soc.* **2000**, *122*, 5879.
[29] K. Dohnalova, A. N. Poddubny, A. A. Prokofiev, W. D. A. M. de Boer, C. P. Umesh, J. M. J. Paulusse, H. Zuilhof, T. Gregorkiewicz, *Light Sci. Appl.* **2013**, *2*, e47.
[30] a) H. Zhang, L. Wang, H. Xiong, L. Hu, B. Yang, W. Li, *Adv. Mater.* **2003**, *15*, 1712; b) D. V. Talapin, A. L. Rogach, E. V. Shevchenko, A. Kornowski, M. Haase, H. Weller, *J. Am. Chem. Soc.* **2002**, *124*, 5782; c) S. Lee, I. Daruka, C. S. Kim, A. L. Barabási, J. L. Merz, J. K. Furdyna, *Phys. Rev. Lett.* **1998**, *81*, 3479.
[31] a) R. Král, K. Nitsch, V. Babin, J. Šulc, H. Jelínková, Y. Yokota, A. Yoshikawa, M. Nikl, *Opt. Mater.* **2013**, *36*, 214; b) L.-N. Sun, J.-B. Yu, G.-L. Zheng, H.-J. Zhang, Q.-G. Meng, C.-Y. Peng, L.-S. Fu, F.-Y. Liu, Y.-N. Yu, *Eur. J. Inorg. Chem.* **2006**, *2006*, 3962.
[32] a) Z. Pan, I. Mora-Seró, Q. Shen, H. Zhang, Y. Li, K. Zhao, J. Wang, X. Zhong, J. Bisquert, *J. Am. Chem. Soc.* **2014**, *136*, 9203; b) R. Rybakiewicz, P. Gawrys, D. Tsikritzis, K. Emmanouil, S. Kennou, M. Zagorska, A. Pron, *Electrochim. Acta* **2013**, *96*, 13.
[33] R. J. Elliott, *Phys. Rev.* **1957**, *108*, 1384.
[34] H. McDaniel, N. Fuke, N. S. Makarov, J. M. Pietryga, V. I. Klimov, *Nat. Commun.* **2013**, *4*, 2887.
[35] Q. Li, J. Wu, Q. Tang, Z. Lan, P. Li, J. Lin, L. Fan, *Electrochem. Commun.* **2008**, *10*, 1299.
[36] a) W. F. Sun, *Nanoscale* **2013**, *5*, 12658; b) W. F. Sun, *Phys. Chem. Chem. Phys.* **2014**, *16*, 5846; c) W. F. Sun, Y. C. Li, W. Xu, Y. W. Mai, *RSC Adv.* **2014**, *4*, 34500.
[37] a) R. Kroon, M. Lenes, J. C. Hummelen, P. W. M. Blom, B. de Boer, *Polym. Rev.* **2008**, *48*, 531; b) M. C. Scharber, D. Mühlbacher, M. Koppe, P. Denk, C. Waldauf, A. J. Heeger, C. J. Brabec, *Adv. Mater.* **2006**, *18*, 789.
[38] a) X. Jin, W. F. Sun, Z. H. Chen, Y. Li, P. J. Li, X. D. He, Y. B. Yuan, S. B. Zou, Y. C. Qin, Q. H. Li, *J. Power Sources* **2014**, *268*, 874; b) X. Jin, W. F. Sun, Z. H. Chen, T. H. Wei, C. Y. Chen, X. D. He, Y. B. Yuan, Y. Li, Q. H. Li, *ACS Appl. Mater. Interfaces* **2014**, *6*, 8771.
[39] a) X. Jin, Q. H. Li, Y. Li, Z. H. Chen, T. H. Wei, X. D. He, W. F. Sun, *Sci. Rep.* **2014**, *4*, 5983; b) Q. H. Li, X. Jin, X. W. Yang, C. Y. Chen, Z. H. Chen, Y. C. Qin, T. H. Wei, W. F. Sun, *Appl. Catal. B* **2015**, *162*, 524.
[40] J. Zhang, C. Yu, L. Wang, Y. Li, Y. Ren, K. Shum, *Sci. Rep.* **2014**, *4*, 6954.
[41] P. R. Brown, D. Kim, R. R. Lunt, N. Zhao, M. G. Bawendi, J. C. Grossman, V. Bulović, *ACS Nano* **2014**, *8*, 5863.
[42] L. Liao, Q. Zhang, Z. Su, Z. Zhao, Y. Wang, Y. Li, X. Lu, D. Wei, G. Feng, Q. Yu, X. Cai, J. Zhao, Z. Ren, H. Fang, F. Robles-Hernandez, S. Baldelli, J. Bao, *Nat. Nanotechnol.* **2014**, *9*, 69.
[43] A. A. Bakulin, J. C. Hummelen, M. S. Pshenichnikov, P. H. M. van Loosdrecht, *Adv. Funct. Mater.* **2010**, *20*, 1653.
[44] D. McMorrow, W. T. Lotshaw, G. A. Kenney-Wallace, *IEEE J. Quant. Electron.* **1988**, *24*, 443.
[45] B. Rand, D. Burk, S. Forrest, *Phys. Rev. B* **2007**, *75*, 115327.
[46] a) S. Sengupta, N. Ganguli, I. Dasgupta, D. D. Sarma, S. Acharya, *Adv. Mater.* **2011**, *23*, 1998; b) D. Zhang, T. Yoshida, K. Furuta, H. Minoura, *J. Photochem. Photobiol. A* **2004**, *164*, 159.